Renewable Energy 178 (2021) 307–317

Contents lists available at ScienceDirect

Renewable Energy

journal homepage: www.elsevier.com/locate/renene

# Carbon nanofiber-supported tantalum oxides as durable catalyst for the oxygen evolution reaction in alkaline media

J.C. Ruiz-Cornejo [a], J.F. Vivo-Vilches [a], D. Sebastián [a, *], M.V. Martínez-Huerta [b], M.J. Lázaro [a, **]

[a] Instituto de Carboquímica, CSIC. Miguel Luesma Castán 4, 50018, Zaragoza, Spain
[b] Instituto de Catálisis y Petroleoquímica, CSIC. Marie Curie 2, 28049, Madrid, Spain

ARTICLE INFO

*Article history:*
Received 21 April 2021
Received in revised form
11 June 2021
Accepted 16 June 2021
Available online 19 June 2021

*Keywords:*
Tantalum
Sodium tantalate
Oxygen evolution reaction
Carbon nanofiber
Electrocatalyst

ABSTRACT

Active and durable electrocatalysts for the oxygen evolution reaction (OER), capable of replacing noble metal catalysts, are required to develop efficient and competitive devices within the frame of the water electrolysis technology for hydrogen production. In this work, we have investigated tantalum based catalysts supported on carbon nanofibers (CNF) for the first time. The effect of CNF characteristics and the catalyst annealing temperature on the electrochemical response for the OER have been analyzed in alkaline environment using a rotating ring disc electrode (RRDE). The best OER activity and oxygen efficiency were found with a highly graphitic CNF, despite its lower surface area, synthesized at 700 °C, and upon a catalyst annealing temperature of 800 °C. The ordering degree of carbon nanofibers favors the production of oxygen in combination with a low oxygen content in tantalum oxides. The most active catalyst exhibited also an excellent durability.



## 1. Introduction

Hydrogen ($H_2$) is widely considered as an ideal candidate to replace fossil fuels and solve the associated problems of pollution and a theoretical future energy crisis. This consideration is supported by its high energy density (33.3 kWh $kg^{-1}$) and by its clean production from the water electrolysis [1]. It is assumed that the worldwide hydrogen demand will grow with the commercialization of fuel cells ensuring the future of sustainable hydrogen economy [2]. Although water electrolysis is a well-studied technology for the splitting of water producing $H_2$ and $O_2$ at low temperatures, the price of $H_2$ production from renewable and sustainable resources is still far from the one needed to be implemented at industrial scale. Therefore, considerable efforts are being made to develop secure and efficient $CO_2$-free production methods to produce $H_2$ at low-cost [3].

Water splitting is a process that involves two half reactions: the oxygen evolution reaction (OER, anode) and the hydrogen evolution reaction (HER, cathode). Under real conditions, water electrolysis needs a greater voltage than the theoretical value of 1.23 V due to the kinetics limitations coming from the anodic reaction (OER), which is a pH−dependent four-electron transfer reaction [4,5]. Noble-metal-based materials, such as Ir, Ru, $IrO_2$ and $RuO_2$, are nowadays the best catalysts in terms of activity and stability in all pH values [6–13]. Nevertheless, their high price and scarcity reduce their attractiveness in practical applications. However, the enhanced electrochemical kinetics of the OER in alkaline environment makes it possible to operate with noble metal-free materials. Different kinds of catalysts have been developed such as oxides and oxyhydroxides of transition metals (e.g. Mn, Co, Ni, Fe) alone or in combination with carbonaceous materials [14–21], and also metal-free carbon-based electrocatalysts [22–24]. These electrocatalysts present great benefits such as relatively low cost and high OER activity. However, their main drawback is related to a poor corrosion and oxidation resistance, particularly of carbon-based materials, which limits their use in a water electrolyzer. To overcome this problem, the design and development of durable and highly active transition metal-based electrocatalysts need to be studied. In this regard, novel carbon nanostructures, such as carbon nanofibers, have shown promising OER performances at the oxygen electrode of metal-air batteries [25].

Tantalum-based catalysts have become popular in water

* Corresponding author.
** Corresponding author.
*E-mail addresses:* dsebastian@icb.csic.es (D. Sebastián), mlazaro@icb.csic.es (M.J. Lázaro).

https://doi.org/10.1016/j.renene.2021.06.076

electrolysis in acidic media. Tantalum is a hard transition metal that is highly corrosion-resistant, which makes it very attractive material in the strongly oxidative environment of the anode [26–32]. However, tantalum oxide alone does not display enough enhancement in performance on OER in acidic media, and needs to be mixed with other metals such as $IrO_2$ [27,29,30]. Today, few reports on tantalum oxide have been conducted in alkaline media. Density functional theory (DFT) calculations revealed that (200)-surface-exposed $Ta_2O_5$ is a suitable candidate to develop OER catalysts with the demanded efficiency, cost and durability in alkaline media for a controlled oxygen environment [33]. According to the simulation, the designated (200)-$Ta_2O_5$ surface has high and durable OER activity. Another successful strategy consisted in the substitution of O atoms by F ones ($TaO_2F$) to tune the electronic structure and, consequently, improve the electrochemical performance [34]. The electrocatalyst showed superior activity and stability toward OER in 1M KOH. Recently, $TaS_2$ nanoflakes have demonstrated efficient activity for OER in acidic and alkaline media, and comparable with $RuO_2$ [35].

In a previous study, catalysts were prepared by using carbon black (Vulcan) as support and depositing the tantalum oxide phase through a microemulsion method [36]. In this case, the optimization of the experimental variables for the microemulsion and the annealing steps, lead to variations in different physicochemical properties of the catalysts such as the oxides/tantalates predominant phases, their crystallinity and the oxygen substoichiometry, which play an important role in the OER electroactivity in alkaline media.

Herein, the role of carbon nanofibers (CNFs) as support has been investigated, taking into account the previous results on the synthesis of tantalum-carbon black catalysts. CNFs possess great versatility due to the possibility of tuning their physical and chemical properties [37]. CNFs stand out for their good structural stability, strength and flexibility as well as good electrical conductivity. All these features are interesting in order to develop active and durable electrodes and catalysts [38,39]. The effects of temperature in the CNF growth and the catalyst annealing have been studied in order to understand how they impact on the electrochemical response of the catalysts for the OER in alkaline environment.

## 2. Experimental section

### 2.1. Synthesis of tantalum-based electrocatalysts

#### 2.1.1. Carbon nanofibers

First the catalyst employed to grow the CNF was synthesized. This catalyst is composed by Ni–Cu–$Al_2O_3$ (Ni:Cu:Al molar proportion of 78:6:16) and was obtained by coprecipitation of the respective metal nitrates, followed by calcination at 450 °C for 8 h and reduction in hydrogen atmosphere at 550 °C for 3 h, which are optimized conditions from a previous work [40]. For the CNF growth, a fixed bed vertical reactor was used, employing 300 mg of catalyst that were heated up under a nitrogen flow. When the desired temperature was reached (600 or 700 °C), methane (Air Products, 99.995%) was fed to the system for 620 min. The cooling process to room temperature was performed in inert atmosphere ($N_2$). The CNFs were named CNF600 and CNF700 according to the growth temperature employed.

#### 2.1.2. Tantalum deposition

Tantalum oxides and sodium tantalates were incorporated on the carbon nanofibers through the modified microemulsion (ME) method developed by our group [36]. Briefly, the organic phase (2.3 g of Igepal CO-520, Aldrich; 20 mL of n-heptane, Honeywell; and 0.75 mL of ethanol 99.5%, Labkem) was mixed with 0.25 mL of 75 mM NaOH (Alfa Aesar), before adding 0.05 mL (0.3 mmol) of tantalum (V) ethoxide (99.98%, Aldrich). The mixture was kept under continuous stirring at room temperature, obtaining the tantalum-based nanoparticles within 5 min. Afterwards, 312 mg of the support was added to the suspension and the mixture was stirred overnight [41]. Both CNF600 and CNF700 were used as support. Materials were then washed with ethanol and water, then dried overnight at 60 °C, before performing the final heat treatment under nitrogen. Two annealing temperatures were studied for each catalyst formulation, 800 and 900 °C, keeping this temperature for 90 min. Lower or higher temperature values were observed to cause a decrease of electrocatalytic activity in a previous work [36]. The catalysts were labeled as TaOxX/CNFY where X is the catalyst annealing temperature (800 or 900 °C) and Y is the CNF growing temperature (600 or 700 °C).

### 2.2. Solid state characterization

The weight percentages for tantalum and nickel were obtained by inductively coupled plasma atomic emission spectroscopy (ICP-OES) in a Xpectroblue-EOP-TI FMT26 (Spectro). The X-ray diffraction (XRD) analyses were made with a Bruker D8 Advance diffractometer with CuKα of 1600 W. Obtained diffractograms were analyzed using FullProf software, fitting the patterns using six different phases (C, Ni, $Ta_2O_5$, $NaTaO_3$, $Na_2Ta_4O_{11}$ and $Na_2Ta_8O_{21}$). X-ray photoelectron spectroscopy (XPS) was employed to determine the metal content on the surface and their oxidation state with an ESCA+ (Omicron) and analyzed using CasaXPS software.

Physisorption analyses were carried out in ASAP2020 (Micromeritics) to obtain nitrogen adsorption-desorption isotherms at −196 °C for the materials. The microporosity was studied by using $N_2$ as adsorbate.

To analyze the surface of the materials, the size of the catalyst nanoparticles and their dispersion, transmission electron microscopy (TEM) and scanning transmission electron microscopy (STEM) micrographs were obtained in a Tecnai F30 -FEI- microscope. To prepare the samples, suspensions of the materials in ethanol were prepared and a few drops were deposited on the grid (Cu coated with carbon film). Histograms for particle size distribution were obtained analyzing the images with ImageJ software. Images of the catalyst after the endurance test were done by recovering the catalyst from the electrode surface with ethanol under sonication. Energy dispersive X-ray (EDX) analysis was carried out in STEM mode to individuate the composition of nanoparticles. Scanning electron microscopy (SEM-EDX) analyses were also obtained in a SEM Hitachi 3400N, EDX Röntec XFlash de Si(Li).

### 2.3. Electrochemical characterization

Regarding the electrochemical tests, a three-electrode setup was employed. The vessel of the cell was filled with 0.1 M NaOH (99.99%, Alfa Aesar) in ultrapure water (Mili-Q, 18.2 MΩ cm). To fabricate the working electrode (WE), an ink of the catalyst was prepared containing 1 mg $mL^{-1}$ of the catalyst, using 50 vol% isopropanol/water as solvent, and Nafion® as binder (30 wt%). Several drops were sequentially deposited and dried on the glassy carbon disk tip (5 mm diameter) of a rotating ring disc electrode (RRDE) to achieve the desired catalyst loading (500 μg $cm^{-2}$). The ring of the RRDE is made of platinum (collection efficiency 0.249). The other two electrodes were a glassy carbon rod as the counter electrode (CE) and a reversible hydrogen electrode (RHE) as the reference (RE).

The catalytic activity for the OER was studied by linear sweep voltammetry (LSV) scanning from 1.0 to 1.9 V vs. RHE at a scan rate

of 5 mV $s^{-1}$ and a rotating speed of 1,600 rpm to favor the diffusion of evolved oxygen. The OER faradaic efficiency was evaluated by setting the ring at 0.6 V vs. RHE to reduce the evolved oxygen. Before OER measurements, cyclic voltammograms (CV) were recorded between 0.05 and 1 V vs. RHE at 20 mV $s^{-1}$ in the deaerated electrolyte. The electrical double layer capacitance was calculated from the CV curves by integrating the area, according to previous works [42].

Endurance tests were performed to evaluate the evolution of the electrode behavior with time. To perform these analyses, cycling chronopotenciometric experiments were performed with intervals of positive and negative current densities (absolute value 1 mA $cm^{-2}$), changing its sign after 180 s or when the cut-off potentials were achieved (1.9 and 0.2 V vs. RHE). A setup was employed similar to the one previously described, but in this case a rotating disk electrode (RDE) with a 5 mm glassy carbon tip was employed and the rotating speed was fixed to 400 rpm.

## 3. Results and discussion

### 3.1. Physico-chemical characterization

The results for the characterization of the supports CNF600 and CNF700 are included in the Supplementary Data. Briefly, both CNFs present a similar XRD pattern (Fig. S.1) with the characteristic peak for graphitic structures (002) at 2θ = 26° (CuKα), which corresponds to a value for lattice parameter c of around 6.8 Å (typical value for CNFs) and the signals for face-centered cubic (FCC) structure of Ni, mainly the peak at around 45° (111). Regarding their porous texture, nitrogen adsorption-desorption isotherms were obtained at −196 °C (Fig. S.2) revealing a larger surface area ($S_{BET}$) and mesopore volume (from Barret-Joyner-Halenda, $V_{BJH}$) for CNF600 ($S_{BET}$ = 136 $m^2$ $g^{-1}$; $V_{BJH}$ = 0.49 $cm^3$ $g^{-1}$) than for CNF700 ($S_{BET}$ = 60 $m^2$ $g^{-1}$; $V_{BJH}$ = 0.23 $cm^3$ $g^{-1}$), while micropore volume is negligible in both samples.

The chemical composition of the electrocatalysts was studied for the bulk materials (ICP) and their most external surface (XPS) (Table 1). ICP analysis showed a larger Ta content for catalysts supported on CNF700 than for the ones synthesized using CNF600. ICP results also showed a small percentage of nickel, 0.9 wt% and 1.8 wt% for CNF600- and CNF700-supported catalysts, respectively, from the CNF growing process even after acid leaching. The weight percentage of Ta in CNF700-supported catalysts is about twice the one in CNF600 ones, indicating that the surface area is not relevant in determining the relative amount of tantalum species adsorbed during the preparation of the catalysts, since CNF600 presents larger surface area than CNF700. This variation in Ta concentration might be thus related to differences in the surface structure of CNF. The average angle between the graphenic layers of the nanofiber and the growth axis changes from 60° to 25° with the increase of temperature [43], resulting in carbon edges exposed on the CNF surface with different interlayer distancing. During the hydrolysis of Ta ethoxide on the surface of CNF, the surface structure of the support appears to be more determining than the surface area to anchor tantalum oxide species.

XPS analyses revealed also a different Ta content in the most external surface of the materials. The Ta 4f core-level of each catalyst is showed in Fig. 1. The Ta $4f_{7/2}$ signal indicates the presence of tantalum oxide at binding energies close to 27 eV, corresponding to Ta (V) oxidation state as found in literature [44] · According to Fig. 1a, there is a peak shift of tantalum oxide between TaOx800/CNF600 (26.9 eV) and TaOx900/CNF600 catalyst (27.2 eV), i.e. with annealing temperature. This shift can be related to the presence of species of Ta in oxidation state lower than +5 according to bibliography [45]. This displacement is negligible in tantalum oxides supported on CNF700 (Fig. 1b). The full spectra are showed in the supplementary information (Fig. S.3).

XRD patterns for the CNF-supported tantalum oxide catalysts were analyzed by means of FullProf software (Fig. 2). Six different phases were detected: carbon and nickel from the support, and four phases containing Ta ($Ta_2O_5$, $NaTaO_3$, $Na_2Ta_4O_{11}$ and $Na_2Ta_8O_{21}$). When the diffractogram for TaOx900/CNF600 (Fig. 2b) was compared to the others, three peaks at 2θ around 32, 35 and 41° that are only present on this one were observed, related to the phase $NaTaO_3$ (purple). In the case of TaOx800/CNF700 (Fig. 2c) and TaOx900/CNF700 (Fig. 2d), the peaks related to the presence of $Ta_2O_5$ (green) resulted the most intense. For the sample TaOx800/CNF600 the ratio between the intensities of the two peaks at 50° was reverse, being the first one related to the presence of $Ta_2O_5$ and $NaTaO_3$, which is less intense than the second one related to $Na_2Ta_4O_{11}$ (orange) for this sample. This is consistent with the fact that, in this sample, there is a larger proportion of Ta in oxidation state IV as denoted by the shift in the signal of the XPS. The values obtained for the lattice parameters of each phase are in good agreement with the ones found in bibliography and similar for all the materials (Table 2). The only significant deviation is the c value in the phase $NaTaO_3$ for TaOx800/CNF700, but the contribution of this phase to the diffractograms is relatively low, so the error for the calculated lattice parameters is larger. The presence of different Ta oxide species has been recently reported to enhance electrocatalytic behavior due to tailored surface modification by creating a charge transfer accumulation at their interface, caused by significant differences in the work function of the Ta species [32].

An attempt of applying the Scherrer equation to calculate the size of the crystals for each phase was made, but due to the fact that there are many phases whose signals appeared at the same value of 2θ made impossible to get reliable results for all of them; therefore, only the values for $Ta_2O_5$ were calculated (Table 3). As expected, the crystallite size increases with the annealing temperature (due to sintering) and is also larger when CNF700 was employed as support (since the amount of $Ta_2O_5$ is much larger in these samples).

Composition of the electrocatalyst nanoparticles was determined by SEM-EDX and XPS, and the O to Ta ratios are summarized in Table 4. At a first glance, values obtained by SEM-EDX do not show a deficiency of oxygen with respect the empiric equation for the different species of tantalum (from O/Ta = 2.5 for $Ta_2O_5$ to 3 for $NaTaO_3$). Nevertheless, it has to be considered that the support has some oxygen (almost 3 at%. measured by XPS), so the value for the catalyst phase should be lower. Regarding XPS, all of the samples present a similar O/Ta ratio, except TaOx800/CNF700, which value is clearly smaller than the others, meaning there is a larger stoichiometric defect in this sample surface. The existence of oxygen defects was related to a favored oxygen adsorption and an enhanced electrocatalytic activity for this kind of materials (metal oxides from groups IV and V of the periodic table) [45].

The morphologies of TaOx800/CNF600 and TaOx800/CNF700 are evaluated through the TEM and STEM images in Fig. 3. Both catalysts show similar fibrous structure from the support with high roughness surface. Nevertheless, it is observed that the particle size of tantalum oxide nanoparticles is influenced by the CNF support. The corresponding histograms in Fig. S.4 show that the average

**Table 1**
Ta and Ni composition in the catalysts obtained by ICP and XPS.

| Catalyst | $\%Ta_{ICP}$ wt.% | $\%Ta_{XPS}$ wt.% | $\%Ni_{ICP}$ wt.% |
|---|---|---|---|
| TaOx800/CNF600 | 8.3 | 10.5 | 0.9 |
| TaOx900/CNF600 | 8.5 | 7.4 | 0.9 |
| TaOx800/CNF700 | 19.2 | 14.3 | 1.8 |
| TaOx900/CNF700 | 20.5 | 14.1 | 1.8 |

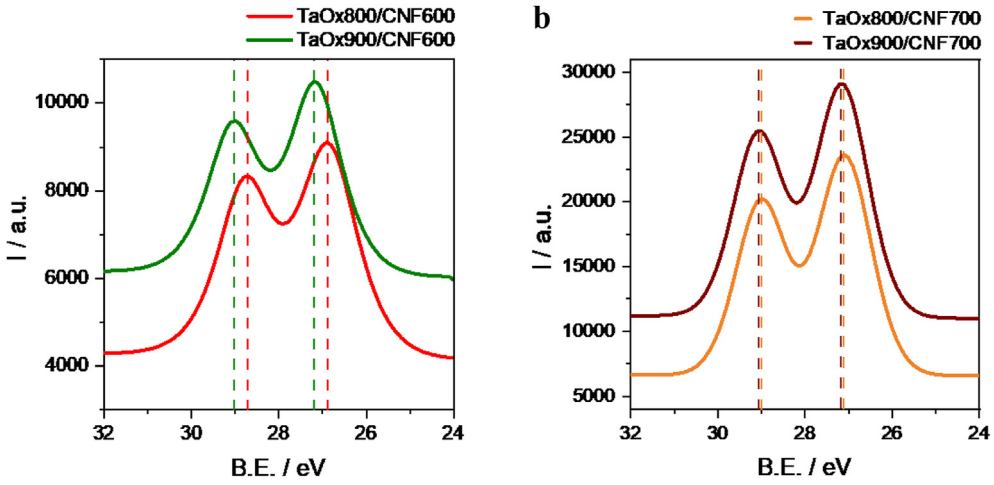


**Fig. 1.** XPS signals for Ta 4f of the catalysts: a) TaOx800/CNF600 (red) and TaOx900/CNF600 (green); b) TaOx800/CNF700 (orange) and TaOx900/CNF700 (brown).

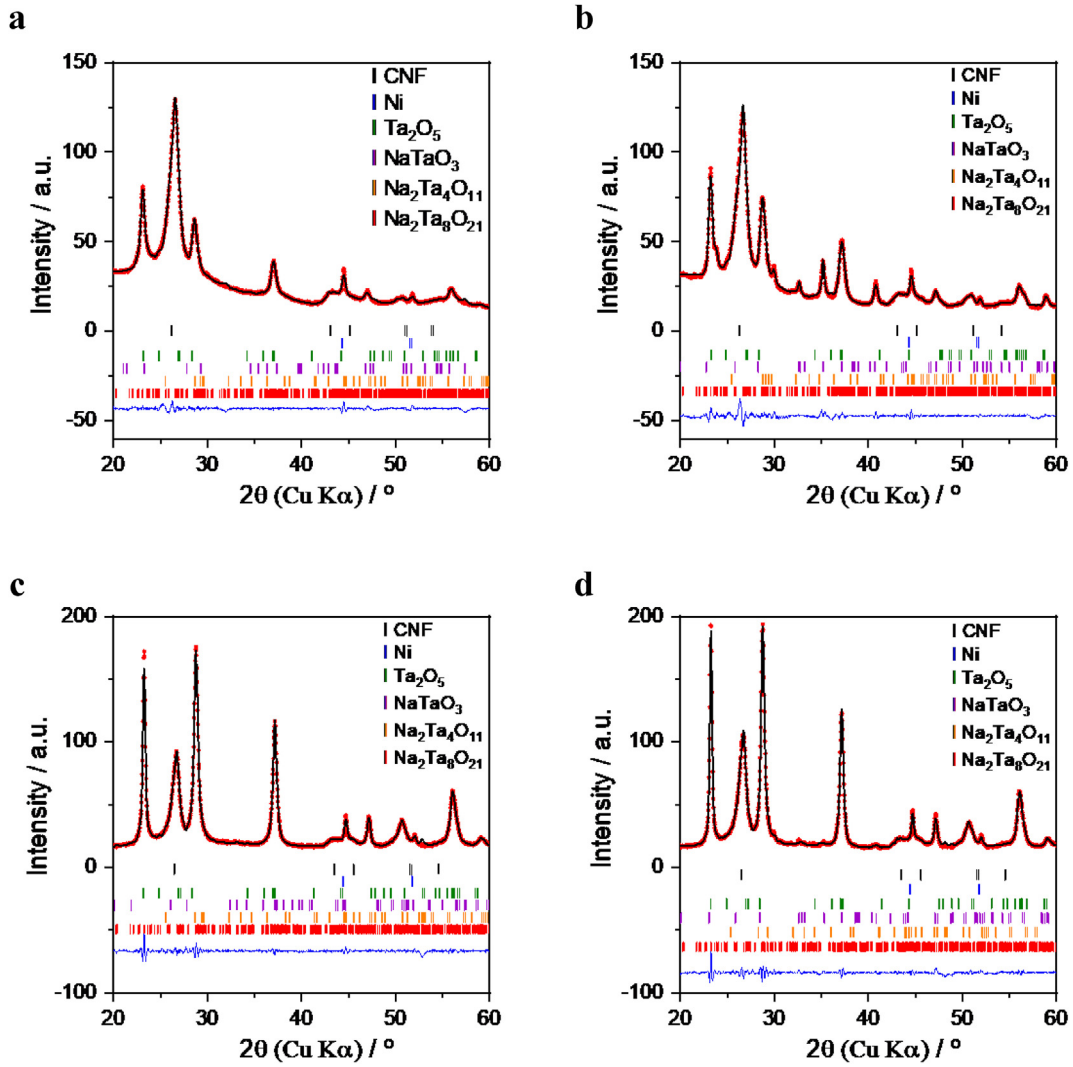


**Fig. 2.** XRD diffractograms for the electrocatalysts. a) TaOx800/CNF600; b) TaOx900/CNF600; c) TaOx800/CNF700; d) TaOx900/CNF700. Experimental points (red); Calculated pattern (black); Error (blue).

**Table 2**
Lattice parameters (L.P.) calculated from XRD for the different electrocatalysts.

| Phase | $Ta_2O_5$ (Pmmm) [46] | | | $NaTaO_3$ (Pnma) [46] | | |
|---|---|---|---|---|---|---|
| L.P. | a/Å | b/Å | c/Å | a/Å | b/Å | c/Å |
| TaOx800/CNF600 | 3.59 | 3.84 | 6.59 | 5.08 | 5.03 | 7.69 |
| TaOx900/CNF600 | 3.58 | 3.82 | 6.57 | 5.40 | 5.50 | 7.80 |
| TaOx800/CNF700 | 3.59 | 3.84 | 6.56 | 5.18 | 5.66 | 8.27 |
| TaOx900/CNF700 | 3.58 | 3.83 | 6.55 | 5.39 | 5.47 | 7.71 |
| Reference value | 3.70 | 3.89 | 6.53 | 5.53 | 5.58 | 7.87 |
| **Phase** | $Na_2Ta_4O_{11}$ (R3c) [47] | | | $Na_2Ta_8O_{21}$ (Pbam) [48] | | |
| **L.P.** | a/Å | b/Å | c/Å | a/Å | b/Å | c/Å |
| TaOx800/CNF600 | 6.23 | 6.23 | 36.67 | 12.37 | 37.44 | 3.94 |
| TaOx900/CNF600 | 6.21 | 6.21 | 36.90 | 12.36 | 37.44 | 3.92 |
| TaOx800/CNF700 | 6.23 | 6.23 | 36.56 | 12.33 | 37.24 | 3.91 |
| TaOx900/CNF700 | 6.32 | 6.32 | 36.63 | 12.35 | 37.26 | 3.91 |
| Reference value | 6.21 | 6.21 | 36.62 | 12.43 | 37.29 | 3.90 |

**Table 3**
Crystallite size of $Ta_2O_5$ phase obtained by XRD. TaOx X/CNF Y (X = annealing temperature in °C; Y= CNF growing temperature in °C).

| | **Crystallite size nm** |
|---|---|
| TaOx800/CNF600 | 11.4 |
| TaOx900/CNF600 | 14.4 |
| TaOx800/CNF700 | 21.7 |
| TaOx900/CNF700 | 26.3 |

**Table 4**
Atomic ratio of oxygen/tantalum obtained by EDX and by XPS.

| Catalyst | O/Ta (SEM-EDX) | O/Ta (XPS) |
|---|---|---|
| TaOx800/CNF600 | 4.00 | 3.55 |
| TaOx900/CNF600 | 4.06 | 4.38 |
| TaOx800/CNF700 | 3.05 | 2.80 |
| TaOx900/CNF700 | 2.90 | 3.47 |

particle size of the TaOx800/CNF600 is smaller than that observed for TaOx800/CNF700. This is in line with the $Ta_2O_5$ crystallite sizes reported in Table 3, although the average diameter from TEM images is slightly lower than the values calculated by XRD. The distribution of the nanoparticles on CNF supports is not very homogeneous, and both samples display some agglomeration of small particles, which explains this difference.

### 3.2. Oxygen evolution reaction (OER)

As CNFs may present an electrocatalytic activity themselves, first tests were performed employing just CNF600 and CNF700 (without tantalum species). Fig. 4 shows the polarization curves at room temperature in 0.1 M NaOH aqueous electrolyte for the supports, revealing some differences in electrocatalytic activity. First, the polarization curve of CNF600 exhibits a small peak at around 1.45 V vs. RHE. To single out the production of oxygen, the Pt ring was set at a constant potential of 0.6 V vs. RHE to reduce the oxygen evolved at the disk. At 1.45 V vs. RHE there is no signal at the ring (Fig. 4b), indicating that the small peak occurring at the disk may be ascribed to the oxidation of metal traces (Ni) used for CNF growth.

Concerning electrocatalytic activity, the signal at the disk (Fig. 4a) is very similar for both materials, indicating similar anodic activity for both nanofibers and considering that both experiments were carried out with the same loading (500 μg $cm^{-2}$). However, the electrical double layer capacitance is quite different, being much larger for CNF600 (4.75 F $g^{-1}$) than for CNF700 (1.04 F $g^{-1}$). The specific capacitances, as an indirect measurement of the electrochemical surface area (ECSA), were determined from cyclic voltammograms, reported in Fig. S.5 (supplementary material), and taking into account the considerations of previous works [42,49]. This way, the intrinsic activity (current normalized by capacitance) is larger for CNF700. On the other hand, the registered ring current for CNF600 is much lower than in the case of CNF700, denoting that the OER electro-catalytic activity is larger for CNF700. Secondary reactions, like the carbon oxidation reaction, might be influencing to some extent the total current registered at the disk. The oxygen efficiency was calculated as in Ref. [50] and considering 4 electrons for the oxygen reduction at the Pt ring. The variation of efficiency with potential is shown in Fig. S.6 (supplementary material), confirming that the oxygen efficiency is about three-fold higher for CNF700. This is in agreement with the higher surface area and roughness of CNF600 together with more surface defects [43], properties that favor a faster carbon oxidation reaction [51–53] and thus a lower oxygen efficiency.

After analyzing the performance of supports, LSV for the different Ta-based CNF-supported electrocatalysts were obtained in the same conditions (Fig. 5). Table 5 summarizes some of the most important electrokinetic parameters with regard to OER, including the onset potential ($E_{onset}$) as determined by the ring current. The results for a commercial $IrO_2$ determined under the same conditions from a previous work [21] as well as a Ta-based catalyst supported on carbon black (Vulcan) [36] are included for the sake of comparison. Firstly, the introduction of tantalum oxide species leads to the improvement of OER activity if compared to the CNF supports alone. With respect to the influence of the catalyst annealing temperature, a lower onset potential at both the disk (upper part of Fig. 5) and the ring (bottom part of Fig. 5) is obtained for electrocatalysts annealed at 800 °C compared to the ones treated at 900 °C, denoting a higher activity for the former catalysts compared to the latter. The physico-chemical characterization of the catalysts pointed out the presence of Ta in oxidation states lower than V when the electrocatalysts were annealed at 800 °C.

The effect of the annealing temperature is clearer in the case of the catalysts supported on CNF600 (Fig. 5a) reducing the onset potential around 30 mV, which is consistent with the shifting to smaller binding energy for the Ta 4f XPS signal in this catalyst, as commented in the previous section. Results for a carbon black-supported catalyst (Vulcan) prepared under the same synthesis conditions and from a previous publication of our group [36] are included in the Fig. 5, showing that all the catalysts obtained in this work present a much higher electrocatalytic activity than the one supported on Vulcan, which points out to the important role of CNF as support on the OER activity.

The enhanced OER activity of TaOx800 catalysts, either supported on CNF600 or CNF700, is also envisaged from the variation of the current at a fixed potential. Table 5 compiles the values of current density at 1.65 V vs. RHE (mA $cm^{-2}$), with TaOx800/CNF600 and TaOx800/CNF700 performing 2–3 folded the current density values of their respective supports alone and being also higher than the counterparts annealed at 900 °C. These catalysts perform even larger current density than the commercial $IrO_2$ (3.18 mA $cm^{-2}$). The electrical double layer capacitance was determined from cyclic voltammetry curves (Fig. S.5) in order to estimate the effect of electrochemical surface area on the OER activity [49]. The specific capacitance values, in F $g^{-1}$, are reported together to the cyclic voltammograms in the supplementary information (Fig. S5). The specific capacitances were larger for the samples supported on CNF600 compared to those based on CNF700 due to the higher BET surface area of the former. Therefore, the normalization of OER current by the capacitance (mA $mF^{-1}$, Table 5) indicates an even larger difference in intrinsic activity between catalysts supported

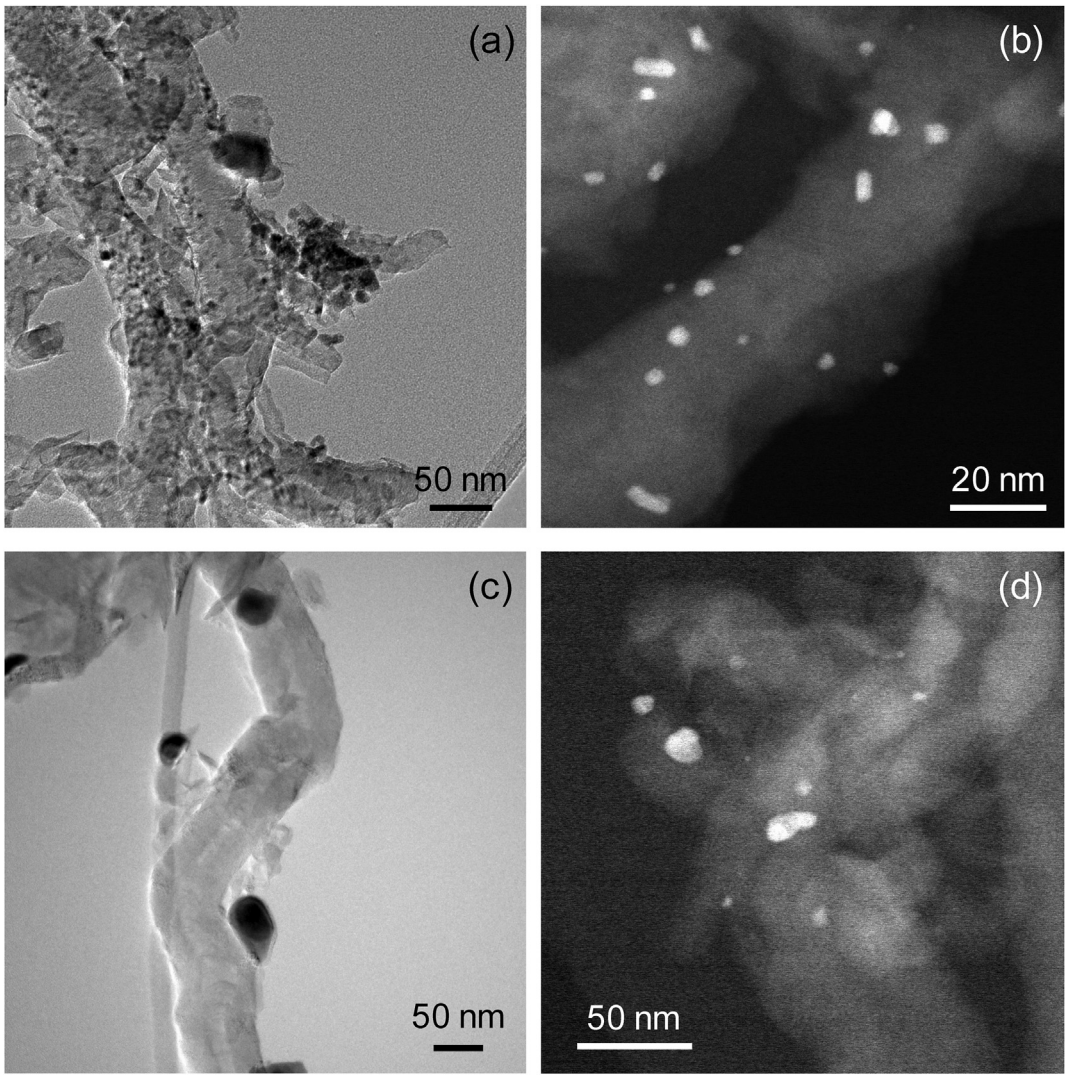


**Fig. 3.** TEM and STEM images with different magnification of a) and b) TaOx800/CNF600 and c) and d) TaOx800/CNF700.

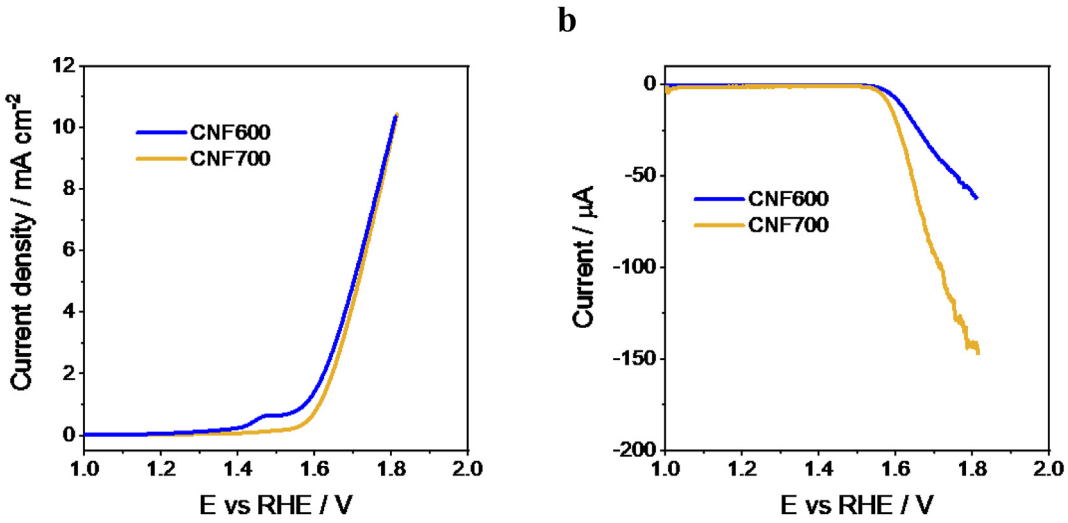


**Fig. 4.** Linear sweep voltammetry at 5 mV $s^{-1}$, 1600 rpm in 0.1 M NaOH. a) Disk current density; b) Ring current. CNF600 (blue); CNF700 (yellow).

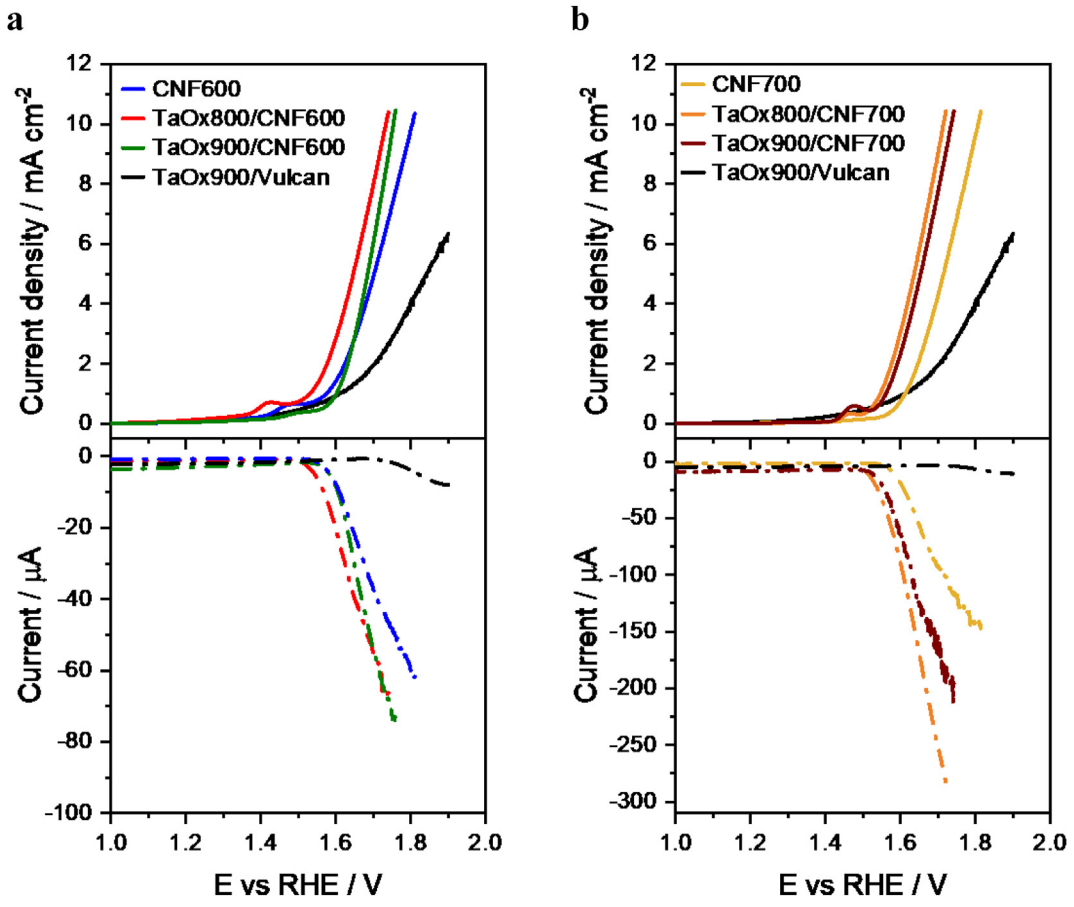


**Fig. 5.** Linear sweep voltammetry at 5 mV $s^{-1}$, 1600 rpm in 0.1 M NaOH. a) Vulcan (black), CNF600 (blue), TaOx800/CNF600 (red), TaOx900/CNF600 (green); b) Vulcan (black), CNF700 (yellow), TaOx800/CNF700 (orange), TaOx900/CNF700 (brown).

**Table 5**
Electro-kinetic parameters for OER including the onset potential ($E_{onset}$), Tafel slope, the exchange current density ($j_0$), the current density at 1.65 V vs. RHE and the overpotential ($\eta$), iR-corrected, at 10 mA $cm^{-2}$.

| Catalyst | $E_{onset}$ (V vs RHE) | Tafel slope (mV $dec^{-1}$) | $j_0$ (mA $cm^{-2}$) | $j_{1.65\ V\ vs\ RHE}$ (mA $cm^{-2}$) | $j_{1.65\ V\ vs\ RHE}$ (mA $mF^{-1}$) | $\eta_{iR\text{-}free,\ 10\ mA\ cm^{-2}}$ (mV) |
|---|---|---|---|---|---|---|
| TaOx800/CNF600 | 1.51 | 114.9 | $2.7 \cdot 10^{-3}$ | 5.21 | 8.4 | 420 |
| TaOx900/CNF600 | 1.54 | 72.8 | $1.0 \cdot 10^{-5}$ | 2.92 | 20.4 | 440 |
| TaOx800/CNF700 | 1.48 | 71.8 | $5.1 \cdot 10^{-5}$ | 5.84 | 106.0 | 405 |
| TaOx900/CNF700 | 1.49 | 79.7 | $8.7 \cdot 10^{-5}$ | 4.83 | 61.9 | 420 |
| CNF600 | 1.54 | 136.2 | $3.3 \cdot 10^{-3}$ | 2.86 | 6.1 | 495 |
| CNF700 | 1.54 | 85.4 | $4.1 \cdot 10^{-5}$ | 2.15 | 21.1 | 495 |
| TaOx900/Vulcan [36] | 1.70 | 304 | $6.2 \cdot 10^{-2}$ | 1.37 | 11.8 | >670[a] |
| $IrO_2$ [21] | 1.53 | – | – | 3.18 | – | 439 |

[a] Not iR corrected.

on CNF600 and on CNF700, with TaOx800/CNF700 presenting the largest intrinsic activity.

The overpotential ($\eta$) at 10 mA $cm^{-2}$ was found to decrease to 405 mV when combining the best tantalum oxide (TaOx800) with the best support (CNF700). From these results it can be concluded that the significant enhancement of OER activity is the result of combining the best support (CNF700) with the appropriate tantalum nanoparticles annealed at 800 °C, i.e. TaOx800/CNF700, since these two aspects individually give lower performing catalysts. The support contributes with an electrically conductive carbonaceous network and a small amount (0.9–1.8 wt%) of Ni nanoparticles, while the tantalum oxides phases contribute with additional active sites for the OER.

Yue and coworkers found overpotentials in the order 480–530 mV for tantalum oxide catalysts [34]. They obtained a significant improvement up to 360 mV when incorporating fluoride to the formulation. Zhang and coworkers also found an improvement in Ta flakes when incorporating sulfur, with an overpotential of 315 mV [35]. With regard to other metals from groups IV and V of the periodic table, there are only a few and recent works reporting OER activity. For example, Kawashima and collaborators evaluated the OER activity of $V_8C_7$, obtaining an overpotential of 458 mV [54]. A catalyst based on HfN presented an overpotential of 358 mV according to the work of Defilippi and coworkers [55]. A better behavior was obtained with a $TiO_2$ nanocomposite with reduced graphene oxide investigated by Hu and collaborators, with an overpotential as low as 283 mV [56]. It is important to point out here that the measurement conditions in these published works

were considerably different (1 M KOH and much larger catalyst loading on the working electrode), since it is well known that hydroxide concentration in the electrolyte and catalyst loading favor the measured electroactivity.

With regard to the effect of carbon support, the catalysts supported on CNF700 (Fig. 5b) presented a higher activity for OER than their counterparts supported on CNF600 (Fig. 5a), as can be seen by comparing activity values in Table 5: i.e. lower $E_{onset}$, higher current density at 1.65 V, and lower overpotential at 10 mA $cm^{-2}$. Interestingly, the CNF700 series of catalysts presents a much higher efficiency to oxygen, as seen from the larger ring currents (bottom part of Fig. 5). The oxygen efficiency for the CNF700 series of catalyst is close to 60% (Fig. S.5), while this value is below 20% for the CNF600 series, highlighting the importance of the carbon support features on OER activity. On the other hand, and according to ICP and XPS, the Ta content on these electro-catalysts is much higher, contributing to a larger density of active sites.

Within the four catalysts prepared, TaOx800/CNF700 is the most active for OER, with the lowest onset potential and the largest current density. For this sample, the main differentiating aspect is that its O/Ta proportion measured by XPS is the smallest of the series. It has been reported that the non-stoichiometry in metal oxides induces defects that are responsible of the electrocatalytic activity [57]. In this context, oxygen substoichiometry has been found of paramount importance in metals of the groups IV and V of the periodic table for the activity towards oxygen reduction reaction, where oxygen vacancies create defects for the adsorption of oxygen [58]. Our experimental evidences point out the importance of having stoichiometric defects of oxygen in the material surface for enhancing the electrocatalytic activity. The onset potential for TaOx800/CNF700 catalyst is 1.48 V vs. RHE, representing an improvement in comparison with $Ta_2O_5$/Carbon black (1.58 V vs. RHE) [34], where the authors stated that the carbon support provides electrical conductivity and improves charge transfer properties of the tantalum phase, promoting the catalytic activity for OER on $Ta_2O_5$.

To better individuate the OER rate determining step (rds) for every catalyst formulation, Tafel plots were examined for both the Ta-based CNF-supported catalysts and the CNF supports without the active phase (Fig. 6), as determined from linear sweep voltammetry curves in Figs. 4 and 5. All the electro-kinetic parameters are summarized in Table 5. First, within the catalysts based on CNF600, there is a significant change in Tafel slope from 136.2 mV $dec^{-1}$ for CNF600 alone to 114.9 and 72.8 mV $dec^{-1}$ for the Ta-based catalysts annealed at 800 °C and 900 °C, respectively. This is a clear indication of the change of the rds with the incorporation of tantalum species. In the case of CNF700-based catalysts, a similar trend was observed, with the Tafel slope decreasing when incorporating tantalum oxides, but in this case, there is not significant difference regarding the temperature at which the electrocatalysts were annealed.

According to the theoretical approach of Shinagawa and coworkers [59] a Tafel slope close to 120 mV $dec^{-1}$ indicates that the reaction rate is determined by any of these situations: (i) the formation of hydroxide is the *rds* (M represents an active site):

$M + OH^- \leftrightarrow MOH + e^-$; *Tafel slope* = 120 mV $dec^{-1}$. (ii) the overpotential exhibits several slopes with 120 mV $dec^{-1}$ occurring at large overpotentials, when the coverage of surface species (MOH, MO, MOOH or $MOO^-$) just before the respective *rds* is high. The first situation, with the formation of hydroxide being the *rds*, is the case for CNF600 and TaOx800/CNF600. A similar conclusion was also found for $CoTiO_3$ supported on nitrogen doped graphene [20].

The Tafel slope at low overpotential was lower than 120 mV $dec^{-1}$ for CNF700 and CNF700-supported catalysts as well as for TaOx900/CNF600, in particular values were found between 70 and 85 mV $dec^{-1}$. In this case, the cause of the Tafel slope decreasing is related to the preferential adsorption of some intermediates generated during different steps of the reaction (MOH, MO, MOOH or MOO-) [59]. Most probably, the presence of different tantalum speciation in the catalysts, as discussed before, leads to active sites acting with different mechanisms, some of them in which the *rds* corresponds to 120 mV $dec^{-1}$ and the other with much lower Tafel slope.

The best activity results were again found for TaOx800/CNF700, characterized by the lowest Tafel slope (71.8 mV $dec^{-1}$) despite presenting lower exchange current density ($j_0$) than other formulations. This highlights the relevance of Tafel slope in determining the OER behavior of this family of catalysts.

### 3.3. Endurance tests

Results for endurance test of the sample with the highest electrocatalytic activity (TaOx800/CNF700) were compared to the ones of our previous work using Vulcan as catalyst support (see Fig. 7)

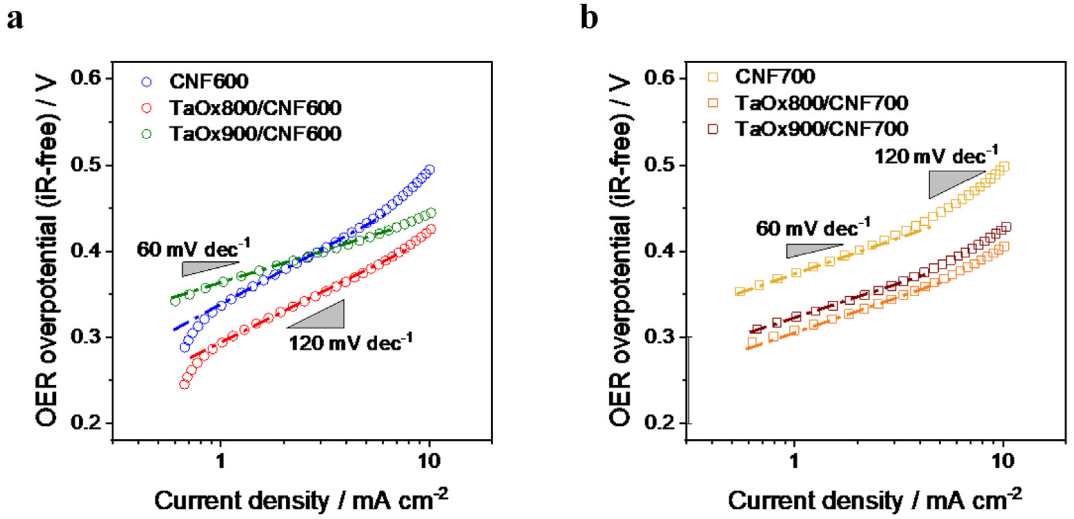


**Fig. 6.** Tafel plots of CNFs and CNF-supported tantalates for the OER from linear sweep voltammetry experiments at 5 mV $s^{-1}$, 1600 rpm in 0.1 M NaOH, the ohmic resistance was estimated from Newman's equation to be 8 Ω $cm^2$. Tafel slopes of 60 and 120 mV $dec^{-1}$ are indicated as reference.

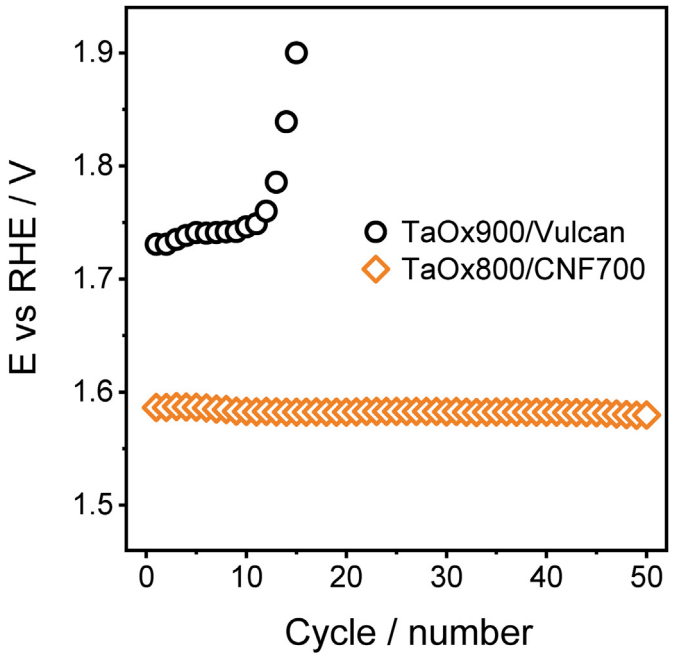


**Fig. 7.** Variation of the potential along successive OER-ORR chronopotentiometric cycles (1 mA $cm^{-2}$) in $O_2$-saturated 0.1M NaOH at 400 rpm. TaOx900/Vulcan (○) and TaOx800/CNF700 (◊).

[36]. While in the case of the TaOx900/Vulcan the onset potential is significantly increased along the first cycles and the cut-off potential is reached after 15 cycles, for TaOx800/CNF700 catalyst this value is maintained all over the 50 cycles tested (150 min OER operation), demonstrating the superior stability of this catalyst.

Fig. 8 shows TEM images of the TaOx800/CNF700 catalyst after the endurance test. The appearance of the carbon nanofiber after durability is the same as found in the catalyst before electrochemical tests (Fig. 3c and d). There are also some nanoparticles ascribed to Ta phases according to EDX analysis (see Fig. S.7). No apparent changes were observed in the catalyst upon the durability test compared to images obtained before the test.

Durability studies of Ta-based catalysts for OER are scarce in the literature. Yue and coworkers found a very good stability in their dioxyfluoride tantalum formulation with graphitized carbon, withstanding 20,000 cyclic voltammetries and chronoamperometry at 1.59 V vs RHE for up to 120h [34], but no information was found about stability of fluoride-free carbon supported Ta catalysts. Unsupported tantalum oxide catalysts ($Ta_2O_5$) showed a very good long-term durability behavior upon potential cycling [33], thus confirming one of the most important features of metals of the IV and V groups in the periodic table as active phase: a high stability under harsh conditions. Therefore, TaOx800/CNF700 electro-catalyst showed a superior performance for OER, not only in terms of activity, but also a higher stability along long-term cycling compared to TaOx900/Vulcan [36] because of the use of nanofibers as supporting material.

## 4. Conclusions

In this work we have synthesized new Ta-based catalysts supported on CNF. The influence of the CNF growing temperature (600 and 700 °C) and the annealing temperature of the catalyst (800 and 900 °C) were investigated. Within the studied materials, TaOx800/CNF700 has shown the best electrochemical activity. This can be explained due to the synergy of two main aspects: the influence of the carbon support, with CNF700 presenting better activity than CNF600 as a material itself; the O/Ta ratio is the lowest of the series (as measured by XPS), showing that the stoichiometric defects of oxygen in the material surface are relevant to improve the electrocatalytic activity. The evolution of current in the ring shows the OER onset potential is close to 1.48 V vs RHE, with a Tafel slope of 72 mV $dec^{-1}$, which are very promising features compared to the most active Ta-based catalysts found in the literature. Additionally, CNF has shown to be a much better support than carbon blacks. CNF as supporting material improves the behavior of the catalyst and also improves its endurance quite significantly. Future studies will be focused on the evaluation of a more extended endurance test and a deep analysis of the activity after cycles using a RRDE.

## CRediT authorship contribution statement

**J.C. Ruiz-Cornejo:** Methodology, Investigation, Data curation, Writing – original draft. **J.F. Vivo-Vilches:** Validation, Data curation, Writing – original draft, Visualization. **D. Sebastián:** Conceptualization, Methodology, Validation, Resources, Writing –

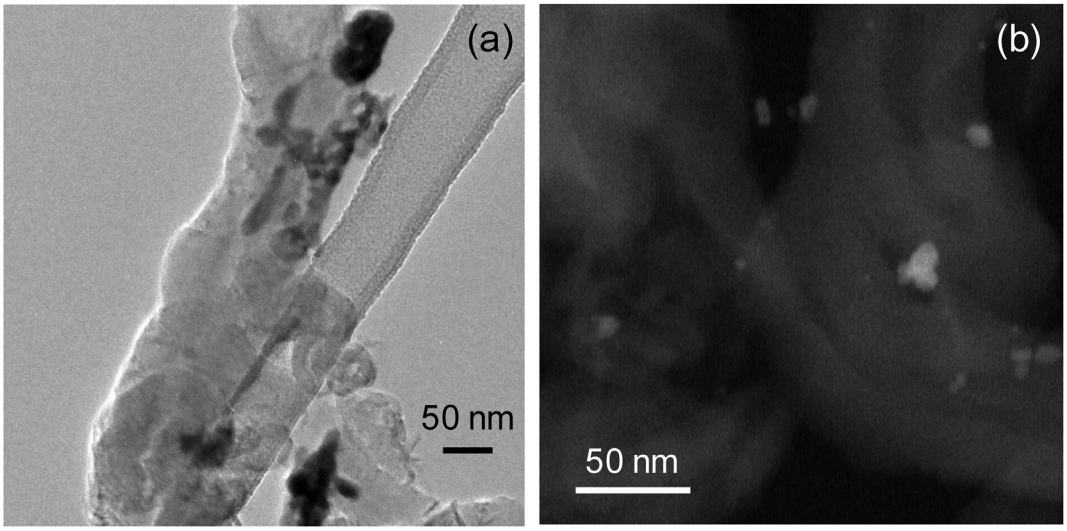


**Fig. 8.** (a) TEM and (b) STEM images with different magnification of TaOx800/CNF700 after endurance test.

review & editing, Visualization. **M.V. Martínez-Huerta:** Supervision, Funding acquisition, Writing – review & editing. **M.J. Lázaro:** Supervision, Project administration, Funding acquisition.

## Declaration of competing interest

The authors declare that they have no known competing financial interests or personal relationships that could have appeared to influence the work reported in this paper.

## Acknowledgements

The authors want to thank the *Ministerio de Economía, Industria y Competitividad* (MICINN) and FEDER for the received funding in the project of reference ENE2017-83976-C2-1-R, and to the *Gobierno de Aragón* (DGA) for the funding to *Grupo de Investigación Conversión de Combustibles* (T06_17R). J.C. Ruiz-Cornejo acknowledges DGA for his PhD grant. D. Sebastián acknowledges the MICINN for the *Ramón y Cajal* research contract (RyC-2016-20944).

## Appendix A. Supplementary data

Supplementary data to this article can be found online at https://doi.org/10.1016/j.renene.2021.06.076.

## References

[1] I. Roger, M.A. Shipman, M.D. Symes, Earth-abundant catalysts for electrochemical and photoelectrochemical water splitting, Nat. Rev. Chem. 1 (2017) 1–13, https://doi.org/10.1038/s41570-016-0003.
[2] M.K. Debe, Electrocatalyst approaches and challenges for automotive fuel cells, Nature 486 (2012) 43–51, https://doi.org/10.1038/nature11115.
[3] S.E. Hosseini, M.A. Wahid, Hydrogen production from renewable and sustainable energy resources: promising green energy carrier for clean development, Renew. Sustain. Energy Rev. 57 (2016) 850–866, https://doi.org/10.1016/j.rser.2015.12.112.
[4] M.E.G. Lyons, S. Floquet, Mechanism of oxygen reactions at porous oxide electrodes. Part 2 - oxygen evolution at RuO2, IrO2 and IrxRu 1-xO2 electrodes in aqueous acid and alkaline solution, Phys. Chem. Chem. Phys. 13 (2011) 5314–5335, https://doi.org/10.1039/c0cp02875d.
[5] X. Shang, B. Dong, Y.M. Chai, C.G. Liu, In-situ electrochemical activation designed hybrid electrocatalysts for water electrolysis, Sci. Bull. 63 (2018) 853–876, https://doi.org/10.1016/j.scib.2018.05.014.
[6] N. Mamaca, E. Mayousse, S. Arrii-Clacens, T.W. Napporn, K. Servat, N. Guillet, K.B. Kokoh, Electrochemical activity of ruthenium and iridium based catalysts for oxygen evolution reaction, Appl. Catal. B Environ. 111–112 (2012) 376–380, https://doi.org/10.1016/j.apcatb.2011.10.020.
[7] Y. Pi, N. Zhang, S. Guo, J. Guo, X. Huang, Ultrathin laminar Ir superstructure as highly efficient oxygen evolution electrocatalyst in broad pH range, Nano Lett. 16 (2016) 4424–4430, https://doi.org/10.1021/acs.nanolett.6b01554.
[8] C.W. Tung, Y.Y. Hsu, Y.P. Shen, Y. Zheng, T.S. Chan, H.S. Sheu, Y.C. Cheng, H.M. Chen, Reversible adapting layer produces robust single-crystal electrocatalyst for oxygen evolution, Nat. Commun. 6 (2015) 1–9, https://doi.org/10.1038/ncomms9106.
[9] R.V. Genova-Koleva, F. Alcaide, G. Álvarez, P.L. Cabot, H.-J. Grande, M.V. Martínez-Huerta, O. Miguel, Supporting IrO2 and IrRuOx nanoparticles on TiO2 and Nb-doped TiO2 nanotubes as electrocatalysts for the oxygen evolution reaction, J. Energy Chem. 34 (2019), https://doi.org/10.1016/j.jechem.2019.03.008.
[10] M. Roca-Ayats, E. Herreros, G. García, M.A. Peña, M.V. Martínez-Huerta, Promotion of oxygen reduction and water oxidation at Pt-based electrocatalysts by titanium carbonitride, Appl. Catal. B Environ. 183 (2016) 53–60, https://doi.org/10.1016/j.apcatb.2015.10.009.
[11] E.J. Kim, J. Shin, J. Bak, S.J. Lee, K. hyun Kim, D.H. Song, J.H. Roh, Y. Lee, H.W. Kim, K.S. Lee, E.A. Cho, Stabilizing role of Mo in TiO2-MoOx supported Ir catalyst toward oxygen evolution reaction, Appl. Catal. B Environ. 280 (2021), https://doi.org/10.1016/j.apcatb.2020.119433.
[12] S. Siracusano, V. Baglio, S.A. Grigoriev, L. Merlo, V.N. Fateev, A.S. Aricò, The influence of iridium chemical oxidation state on the performance and durability of oxygen evolution catalysts in PEM electrolysis, J. Power Sources 366 (2017) 105–114, https://doi.org/10.1016/j.jpowsour.2017.09.020.
[13] S. Siracusano, N. Van Dijk, E. Payne-Johnson, V. Baglio, A.S. Aricò, Nanosized IrOx and IrRuOx electrocatalysts for the O2 evolution reaction in PEM water electrolysers, Appl. Catal. B Environ. 164 (2015) 488–495, https://doi.org/10.1016/j.apcatb.2014.09.005.
[14] Y. Yang, K. Zhou, L. Ma, Y. Liang, X. Yang, Z. Cui, S. Zhu, Z. Li, Free-standing ternary NiWP film for efficient water oxidation reaction, Appl. Surf. Sci. 434 (2018) 871–878, https://doi.org/10.1016/j.apsusc.2017.10.049.
[15] Y. Wang, T. Zhou, K. Jiang, P. Da, Z. Peng, J. Tang, B. Kong, W.-B. Cai, Z. Yang, G. Zheng, Reduced mesoporous Co $_3$ O $_4$ nanowires as efficient water oxidation electrocatalysts and supercapacitor electrodes, Adv. Energy Mater. 4 (2014) 1400696, https://doi.org/10.1002/aenm.201400696.
[16] K. Fominykh, J.M. Feckl, J. Sicklinger, M. Döblinger, S. Böcklein, J. Ziegler, L. Peter, J. Rathousky, E.-W. Scheidt, T. Bein, D. Fattakhova-Rohlfing, Ultrasmall dispersible crystalline nickel oxide nanoparticles as high-performance catalysts for electrochemical water splitting, Adv. Funct. Mater. 24 (2014) 3123–3129, https://doi.org/10.1002/adfm.201303600.
[17] Y. Cheng, S.P. Jiang, Advances in electrocatalysts for oxygen evolution reaction of water electrolysis-from metal oxides to carbon nanotubes, Prog. Nat. Sci. Mater. Int. 25 (2015) 545–553, https://doi.org/10.1016/j.pnsc.2015.11.008.
[18] M. Gao, W. Sheng, Z. Zhuang, Q. Fang, S. Gu, J. Jiang, Y. Yan, Efficient water oxidation using nanostructured α-nickel-hydroxide as an electrocatalyst, J. Am. Chem. Soc. 136 (2014) 7077–7084, https://doi.org/10.1021/ja502128j.
[19] B. Aghabarari, J.M. Luque-Centeno, M. Capel-Sánchez, M.J.L. Elorri, M.V. Martínez-Huerta, Ni-based composites from chitosan biopolymer a one-step synthesis for oxygen evolution reaction, Catalysts 9 (2019), https://doi.org/10.3390/catal9050471.
[20] J.M. Luque-Centeno, M.V. Martínez-Huerta, D. Sebastián, J.I. Pardo, M.J. Lázaro, CoTiO3/NrGO nanocomposites for oxygen evolution and oxygen reduction reactions: synthesis and electrocatalytic performance, Electrochim. Acta 331 (2020) 135396, https://doi.org/10.1016/j.electacta.2019.135396.
[21] J.M. Luque-Centeno, M.V. Martínez-Huerta, D. Sebastián, G. Lemes, E. Pastor, M.J. Lázaro, Bifunctional N-doped graphene Ti and Co nanocomposites for the oxygen reduction and evolution reactions, Renew. Energy 125 (2018) 182–192, https://doi.org/10.1016/j.renene.2018.02.073.
[22] Y.P. Zhu, Y. Jing, A. Vasileff, T. Heine, S.Z. Qiao, 3D synergistically active carbon nanofibers for improved oxygen evolution, Adv. Energy Mater. 7 (2017) 1602928, https://doi.org/10.1002/aenm.201602928.
[23] Z. Lijun, Z. Chunyan, C. Xiaoyi, Q. Yao, J. Haifeng, L. Baosheng, L. Linfei, S. Zexiang, H. Wei, P. N, Co-doped hierarchical porous graphene as a metal-free bifunctional air cathode for Zn–Air batteries, ChemElectroChem 5 (2018) 1811–1816, https://doi.org/10.1002/celc.201701148.
[24] J. Zhao, Y. Liu, X. Quan, S. Chen, H. Zhao, H. Yu, Nitrogen and sulfur co-doped graphene/carbon nanotube as metal-free electrocatalyst for oxygen evolution reaction: the enhanced performance by sulfur doping, Electrochim. Acta 204 (2016) 169–175, https://doi.org/10.1016/j.electacta.2016.04.034.
[25] Y.J. Wang, H. Fan, A. Ignaszak, L. Zhang, S. Shao, D.P. Wilkinson, J. Zhang, Compositing doped-carbon with metals, non-metals, metal oxides, metal nitrides and other materials to form bifunctional electrocatalysts to enhance metal-air battery oxygen reduction and evolution reactions, Chem. Eng. J. 348 (2018) 416–437, https://doi.org/10.1016/j.cej.2018.04.208.
[26] F. Karimi, B.A. Peppley, Metal carbide and oxide supports for iridium-based oxygen evolution reaction electrocatalysts for polymer-electrolyte-membrane water electrolysis, Electrochim. Acta 246 (2017) 654–670, https://doi.org/10.1016/j.electacta.2017.06.048.
[27] F. Amano, Y. Furusho, Y.M. Hwang, Amorphous iridium and tantalum oxide layers coated on titanium felt for electrocatalytic oxygen evolution reaction, ACS Appl. Energy Mater. 3 (2020) 4531–4538, https://doi.org/10.1021/acsaem.0c00208.
[28] A.V. Nikiforov, I.M. Petrushina, E. Christensen, A.L. Tomás-García, N.J. Bjerrum, Corrosion behaviour of construction materials for high temperature steam electrolysers, Int. J. Hydrogen Energy 36 (2011) 111–119, https://doi.org/10.1016/j.ijhydene.2010.09.023.
[29] H. Lv, G. Zhang, C. Hao, C. Mi, W. Zhou, D. Yang, B. Li, C. Zhang, Activity of IrO2 supported on tantalum-doped TiO2 electrocatalyst for solid polymer electrolyte water electrolyzer, RSC Adv. 7 (2017) 40427–40436, https://doi.org/10.1039/c7ra06534e.
[30] J.M. Hu, H.M. Meng, J.Q. Zhang, C.N. Cao, Degradation mechanism of long service life Ti/IrO2–Ta2O5 oxide anodes in sulphuric acid, Corrosion Sci. 44 (2002) 1655–1668, https://doi.org/10.1016/S0010-938X(01)00165-2.
[31] J. Polonský, P. Mazúr, M. Paidar, E. Christensen, K. Bouzek, Performance of a PEM water electrolyser using a TaC-supported iridium oxide electrocatalyst, Int. J. Hydrogen Energy 39 (2014) 3072–3078, https://doi.org/10.1016/j.ijhydene.2013.12.085.
[32] G. Zhang, D. Sebastián, X. Zhang, Q. Wei, C. Lo Vecchio, J. Zhang, V. Baglio, W. Wang, S. Sun, A.S. Aricò, A.C. Tavares, Engineering of a low-cost, highly active, and durable tantalate–graphene hybrid electrocatalyst for oxygen reduction, Adv. Energy Mater. 2000075 (2020) 1–11, https://doi.org/10.1002/aenm.202000075.
[33] W. Xiao, X. Huang, W. Song, Y. Yang, T.S. Herng, J.M. Xue, Y.P. Feng, J. Ding, High catalytic activity of oxygen-induced (200) surface of Ta2O5 nanolayer towards durable oxygen evolution reaction, Nano Energy 25 (2016) 60–67, https://doi.org/10.1016/j.nanoen.2016.04.020.
[34] X. Yue, Y. Jin, P.K. Shen, Highly stable and efficient non-precious metal electrocatalysts of tantalum dioxyfluoride used for the oxygen evolution reaction, J. Mater. Chem. A. 5 (2017) 8287–8291, https://doi.org/10.1039/C7TA01838J.
[35] M. Zhang, Y. He, D. Yan, H. Xu, A. Wang, Z. Chen, S. Wang, H. Luo, K. Yan, Multifunctional 2H-TaS2 nanoflakes for efficient supercapacitors and electrocatalytic evolution of hydrogen and oxygen, Nanoscale 11 (2019) 22255–22260, https://doi.org/10.1039/c9nr07564j.
[36] J.C. Ruiz-Cornejo, D. Sebastián, M.V. Martínez-Huerta, M.J. Lázaro, Tantalum-

based electrocatalysts prepared by a microemulsion method for the oxygen reduction and evolution reactions, Electrochim. Acta 317 (2019) 261–271, https://doi.org/10.1016/j.electacta.2019.05.145.
[37] J.C. Ruiz-Cornejo, D. Sebastián, M.J. Lázaro, Synthesis and applications of carbon nanofibers: a review, Rev. Chem. Eng. 36 (2020) 493–511, https://doi.org/10.1515/revce-2018-0021.
[38] H. Gu, Y. Huang, L. Zuo, W. Fan, T. Liu, Graphene sheets wrapped carbon nanofibers as a highly conductive three-dimensional framework for perpendicularly anchoring of MoS2: advanced electrocatalysts for hydrogen evolution reaction, Electrochim. Acta 219 (2016) 604–613, https://doi.org/10.1016/j.electacta.2016.10.015.
[39] Q. Ding, M. Liu, Y.E. Miao, Y. Huang, T. Liu, Electrospun nickel-decorated carbon nanofiber membranes as efficient electrocatalysts for hydrogen evolution reaction, Electrochim. Acta 159 (2015) 1–7, https://doi.org/10.1016/j.electacta.2015.01.197.
[40] I. Suelves, M.J. Lázaro, R. Moliner, Y. Echegoyen, J.M. Palacios, Characterization of NiAl and NiCuAl catalysts prepared by different methods for hydrogen production by thermo catalytic decomposition of methane, Catal. Today 116 (2006) 271–280, https://doi.org/10.1016/j.cattod.2006.05.071.
[41] M.H. Oh, N. Lee, H. Kim, S.P. Park, Y. Piao, J. Lee, S.W. Jun, W.K. Moon, S.H. Choi, T. Hyeon, Large-scale synthesis of bioinert tantalum oxide nanoparticles for X-ray computed tomography imaging and bimodal image-guided sentinel lymph node mapping, J. Am. Chem. Soc. 133 (2011) 5508–5515, https://doi.org/10.1021/ja200120k.
[42] D. Torres, S. Pérez-Rodríguez, D. Sebastián, J.L. Pinilla, M.J. Lázaro, I. Suelves, Capacitance enhancement of hydrothermally reduced graphene oxide nanofibers, Nanomaterials 10 (2020) 1–17, https://doi.org/10.3390/nano10061056.
[43] D. Sebastián, A.G. Ruiz, I. Suelves, R. Moliner, M.J. Lázaro, On the importance of the structure in the electrical conductivity of fishbone carbon nanofibers, J. Mater. Sci. 48 (2013) 1423–1435, https://doi.org/10.1007/s10853-012-6893-1.
[44] N. Benito, C. Palacio, Nanostructuring of Ta 2 O 5 surfaces by low energy Ar + bombardment, Appl. Surf. Sci. 351 (2015) 753–759, https://doi.org/10.1016/j.apsusc.2015.05.143.
[45] H. Imai, M. Matsumoto, T. Miyazaki, S. Fujieda, A. Ishihara, M. Tamura, K. Ota, Structural defects working as active oxygen-reduction sites in partially oxidized Ta-carbonitride core-shell particles probed by using surface-sensitive conversion-electron-yield x-ray absorption spectroscopy, Appl. Phys. Lett. 96 (2010) 191905, https://doi.org/10.1063/1.3430543.
[46] A. Jain, S.P. Ong, G. Hautier, W. Chen, W.D. Richards, S. Dacek, S. Cholia, D. Gunter, D. Skinner, G. Ceder, K.A. Persson, Commentary: the materials project: a materials genome approach to accelerating materials innovation, Apl. Mater. 1 (2013), 011002, https://doi.org/10.1063/1.4812323.
[47] P. Cerny, T.S. Ercit, Some recent advances in the mineralogy and geochemistry of Nb and Ta in rare-element granitic pegmatites, Bull. Mineral. 108 (1985) 499–532, https://doi.org/10.3406/bulmi.1985.7846.
[48] J.-P. Chaminade, M. Pouchard, P. Hagenmuller, Tantalates et oxyfluorotantalates de sodium, Rev. Chim. Miner. 9 (1972) 381–402, doi:hal-00125096.
[49] G. Li, L. Anderson, Y. Chen, M. Pan, P.Y. Abel Chuang, New insights into evaluating catalyst activity and stability for oxygen evolution reactions in alkaline media, Sustain. Energy Fuels 2 (2018) 237–251, https://doi.org/10.1039/c7se00337d.
[50] I.S. Filimonenkov, C. Bouillet, G. Kéranguéven, P.A. Simonov, G.A. Tsirlina, E.R. Savinova, Carbon materials as additives to the OER catalysts: RRDE study of carbon corrosion at high anodic potentials, Electrochim. Acta 321 (2019) 134657, https://doi.org/10.1016/j.electacta.2019.134657.
[51] C. Alegre, D. Sebastián, M.J. Lázaro, Carbon xerogels electrochemical oxidation and correlation with their physico-chemical properties, Carbon N. Y. 144 (2019) 382–394, https://doi.org/10.1016/j.carbon.2018.12.065.
[52] S. Pérez-Rodríguez, D. Sebastián, M.J. Lázaro, Electrochemical oxidation of ordered mesoporous carbons and the influence of graphitization, Electrochim. Acta 303 (2019) 167–175, https://doi.org/10.1016/j.electacta.2019.02.065.
[53] S. Pérez-Rodríguez, D. Sebastián, M.J. Lázaro, Insights on the electrochemical oxidation of ordered mesoporous carbons, J. Electrochem. Soc. 167 (2020), 024511, https://doi.org/10.1149/1945-7111/ab6a8f.
[54] K. Kawashima, C.L. Cao, H. Li, R.A. Márquez-Montes, B.R. Wygant, Y.J. Son, J.V. Guerrera, G. Henkelman, C.B. Mullins, Evaluation of a V8C7Anode for oxygen evolution in alkaline media: unusual morphological behavior, ACS Sustain. Chem. Eng. 8 (2020) 14101–14108, https://doi.org/10.1021/acssuschemeng.0c04759.
[55] C. Defilippi, D.V. Shinde, Z. Dang, L. Manna, C. Hardacre, A.J. Greer, C. D'Agostino, C. Giordano, HfN nanoparticles: an unexplored catalyst for the electrocatalytic oxygen evolution reaction, Angew. Chem. Int. Ed. 58 (2019) 15464–15470, https://doi.org/10.1002/anie.201908758.
[56] Y. Hu, T. Ding, K. Zhang, B. Li, B. Zhu, K. Tang, Component-tunable rutile-anatase TiO2/reduced graphene oxide nanocomposites for enhancement of electrocatalytic oxygen evolution, ChemNanoMat 4 (2018) 1133–1139, https://doi.org/10.1002/cnma.201800252.
[57] D. Chen, C. Chen, Z.M. Baiyee, Z. Shao, F. Ciucci, Nonstoichiometric oxides as low-cost and highly-efficient oxygen reduction/evolution catalysts for low-temperature electrochemical devices, Chem. Rev. 115 (2015) 9869–9921, https://doi.org/10.1021/acs.chemrev.5b00073.
[58] A. Ishihara, Y. Ohgi, K. Matsuzawa, S. Mitsushima, K. Ota, Progress in non-precious metal oxide-based cathode for polymer electrolyte fuel cells, Electrochim. Acta 55 (2010) 8005–8012, https://doi.org/10.1016/j.electacta.2010.03.002.
[59] T. Shinagawa, A.T. Garcia-Esparza, K. Takanabe, Insight on Tafel slopes from a microkinetic analysis of aqueous electrocatalysis for energy conversion, Sci. Rep. 5 (2015) 1–21, https://doi.org/10.1038/srep13801.